Flow Visualization of Density in a Cryogenic Wind Tunnel Using Planar Rayleigh and Raman Scattering

Gregory C. Herring and Behrooz Shirinzadeh
Langley Research Center, Hampton, Virginia

The NASA STI Program Office . . . in Profile

Since its founding, NASA has been dedicated to the advancement of aeronautics and space science. The NASA Scientific and Technical Information (STI) Program Office plays a key part in helping NASA maintain this important role.

The NASA STI Program Office is operated by Langley Research Center, the lead center for NASA's scientific and technical information. The NASA STI Program Office provides access to the NASA STI Database, the largest collection of aeronautical and space science STI in the world. The Program Office is also NASA's institutional mechanism for disseminating the results of its research and development activities. These results are published by NASA in the NASA STI Report Series, which includes the following report types:

*   TECHNICAL PUBLICATION. Reports of completed research or a major significant phase of research that present the results of NASA programs and include extensive data or theoretical analysis. Includes compilations of significant scientific and technical data and information deemed to be of continuing reference value. NASA counterpart of peer-reviewed formal professional papers, but having less stringent limitations on manuscript length and extent of graphic presentations.

*   TECHNICAL MEMORANDUM. Scientific and technical findings that are preliminary or of specialized interest, e.g., quick release reports, working papers, and bibliographies that contain minimal annotation. Does not contain extensive analysis.

*   CONTRACTOR REPORT. Scientific and technical findings by NASA-sponsored contractors and grantees.

*   CONFERENCE PUBLICATION. Collected papers from scientific and technical conferences, symposia, seminars, or other meetings sponsored or co-sponsored by NASA.

*   SPECIAL PUBLICATION. Scientific, technical, or historical information from NASA programs, projects, and missions, often concerned with subjects having substantial public interest.

TECHNICAL TRANSLATION. English-language translations of foreign scientific and technical material pertinent to NASA's mission.

Specialized services that complement the STI Program Office's diverse offerings include creating custom thesauri, building customized databases, organizing and publishing research results . . . even providing videos.

For more information about the NASA STI Program Office, see the following:

*   Access the NASA STI Program Home Page at *http://www.sti.nasa.gov*

*   Email your question via the Internet to help@sti.nasa.gov

*   Fax your question to the NASA STI Help Desk at (301) 621-0134

*   Telephone the NASA STI Help Desk at (301) 621-0390

*   Write to:
    NASA STI Help Desk
    NASA Center for AeroSpace Information
    7121 Standard Drive
    Hanover, MD 21076-1320

Flow Visualization of Density in a Cryogenic Wind Tunnel Using Planar Rayleigh and Raman Scattering

Gregory C. Herring and Behrooz Shirinzadeh
Langley Research Center, Hampton, Virginia

June 2002

Acknowledgments

We thank W. E. Lipford and M. T. Fletcher for help with the installation of the laser setup, A. Seifert and L. G. Pack for helpful discussions, and M. Kulick for fabrication of the modified off-block.

Abstract

Using a pulsed Nd:YAG laser (532 nm) and a gated, intensified charge-coupled device, planar Rayleigh and Raman scattering techniques have been used to visualize the unseeded Mach 0.2 flow density in a 0.3-meter transonic cryogenic wind tunnel. Detection limits are determined for density measurements by using both unseeded Rayleigh and Raman (N_2 vibrational) methods. Seeding with CO_2 improved the Rayleigh flow visualization at temperatures below 150 K. The seeded Rayleigh version was used to demonstrate the observation of transient flow features in a separated boundary layer region, which was excited with an oscillatory jet. Finally, a significant degradation of the laser light sheet, in this cryogenic facility, is discussed.

Introduction

NASA Langley Research Center (LaRC) has an ongoing effort (see citations in ref. 1) for the development of Rayleigh scattering (ref. 2) in a variety of wind tunnels. Many wind tunnels, including LaRC's 0.3-Meter Transonic Cryogenic Tunnel (TCT), operate near the condensation point of the working fluid; hence, clusters of molecules may form in the unseeded flow. With clusters, the quantitative aspect of the density measurement from the Rayleigh signal is compromised. Since the Rayleigh scatter is elastic and proportional to the sixth power of the cluster size, the scatter from the clusters can easily be larger than the molecular scatter. Since the cluster-size distribution is not typically known, the density of molecular scatters is hard to deconvolve from the cluster signal. In this case, Rayleigh scattering cannot easily measure flow density and is limited to qualitative flow visualization. Recently, (ref. 3) it was demonstrated that clustering does not occur in the free-stream flow for typical run conditions in the TCT, making Rayleigh scattering one promising method for quantitative density measurements in the TCT.

In this report, planar imaging of density in the unseeded flow is demonstrated in the TCT with Rayleigh scattering from a laser beam formed into a sheet. Seeding CO_2 into the flow is shown to induce clustering in the flow medium, increasing the magnitude of the elastic light scattering and enhancing the quality of the images. This seeded version of planar Rayleigh scattering is used to detect transient flow structure downstream of the blowing slot in a near-zero-mass-flow oscillatory blowing experiment. Planar Raman scattering from the 0-1 vibrational transition in N_2 is also demonstrated as a second potential method to visualize the unseeded flow. Finally, beam steering effects, by the cryogenic fluid in TCT, are described.

The elastic light scatter is in the Rayleigh regime for the unseeded flow; however, adding CO_2 to induce clusters raises questions about the size of the clusters and whether the seeded elastic light scatter is in the Rayleigh or Mie regime. For the purpose of this work, it is not important if the elastic scatter is in the Rayleigh or Mie regime, and we will hereafter refer to the seeded scattering as Rayleigh scattering.

Rayleigh and Raman Scattering

A summary of Rayleigh and Raman scattering is given in reference 4. The scattered light signal P (photoelectrons/sec) is given by

$$P = N(d\sigma/d\Omega)_{90} \, L \, P_1 \, \varepsilon \, \eta \, \Omega \tag{1}$$

The symbols are the solid angle Ω (sr) used to collect the signal, the transmission η of the collection optics from the sample volume to the detector cathode, the incident power P_l (photons/sec) of the laser beam in the sample volume, the quantum efficiency ε of the detector cathode, the length L (m) of the laser beam that is imaged on the detector, the differential scattering cross section per molecule $(d\sigma/d\Omega)_{90}$ (m^2/sr molecule) at 90° to the polarization direction and 90° to the beam propagation direction, and the number density N (molecules/m^3) of the scattering medium.

Typically, the Rayleigh cross section is 10^3 times larger than the Raman cross section; hence, Rayleigh signals are large compared to Raman signals. However, because Rayleigh scattering is elastic, scattered laser light from windows and walls produces a background level that interferes with the Rayleigh signal. Fluctuations in that background typically appear as the dominant noise on the Rayleigh signal. In contrast, the Raman signal is inelastic, shifted in energy by 2330 cm^{-1} in the case of the N_2 0-1 vibrational band that is used here. For laser excitation at 532 nm, a narrow-band interference filter, centered at 607 nm, can be used to block the scattered light at the laser frequency. Thus, scattered light is minimal, and shot noise and dark current typically dominate the noise in the signal-to-noise ratio (SNR) of the Raman signal.

Experimental Setup

Wind Tunnel

This work was performed at the 0.3-m TCT at LaRC. It is a fan-driven, closed-circuit facility (ref. 5) designed to achieve large Reynolds numbers ($\sim 3 \times 10^8$/m) by using high-pressure ($\sim 5 \times 10^5$ MPa) and low-temperature (~ 100 K) N_2 as the flow medium. This two-dimensional tunnel has a test section width of 33 cm and is used primarily for the testing of airfoil configurations.

The model consists of a 2.6-cm hump that is mounted on the sidewall. This configuration simulates the 2-dimensional flow over the upper surface of an airfoil. The hump model is described further in reference 6. The oscillatory excitation experiment of reference 6 was designed to study the delay of flow separation from a simulated airfoil at Mach 0.2 in a high Reynolds number flow. A sketch of the hump model and laser light sheet is shown in figure 1. The slot S2 is for oscillatory excitation of the flowfield. Near-room-temperature N_2 was used as the driving fluid. There is typically a slight bias on the oscillatory flow through slot S2 in favor of a small mass flow into the tunnel. This net mass flow into the tunnel is small relative to the mass flow of the free-stream of the test section. In this study, after demonstrating that we could visualize the unseeded flow, gaseous CO_2 was seeded into the relatively warm N_2 fluid that is injected into the cold flow through the slot S2. The CO_2 induces clustering and greatly increases the strength of the scattered Rayleigh light.

For typical operation, the facility is cooled significantly below room temperature and will move 3 cm relative to the concrete floor. Thus the laser, camera, and all optics are mounted directly on the tunnel to maintain their position relative to the model during this thermal contraction. Upon cooling and pressurizing, it was necessary to repeatedly enter the test cell and adjust the optical alignment. Since the outer window W2 is cold, it is necessary to purge the window surface with dry N_2 to avoid the water condensation. Since the Rayleigh and Raman scattered light is relatively small, it is important to have a good-quality purge since the slightest amount of condensation can degrade the Rayleigh images. The laser-beam path outside the tunnel should be shielded from the fog generated from the low-temperature air in the test cell.

Optical Arrangement

The facility/model geometry and the limited optical access determined the observation region. The optical and electronic setup is similar to one used previously (ref. 7), with the exception that the excimer laser of reference 7 is replaced with a Quanta Ray DCR-1 Nd:YAG laser. Because of uncertainty in the 266-nm transmission of the tunnel windows, we used 532 nm in this preliminary work. In future work, an ultraviolet (UV) laser should improve the SNR, relative to that obtained in this work. The Rayleigh and Raman signals will increase significantly with decreasing laser wavelength, and steel models absorb UV relatively better than visible light, reducing stray light.

The Nd:YAG laser is frequency doubled (i.e., 532 nm) and produces 8-ns-long pulses at a 10-Hz repetition rate. This short pulse width freezes all fluid motion and gives instantaneous images of the flow density. Schematics of the optical apparatus are shown in figures 2(a) and 2(b). Figure 2(a) shows a top view, including the plenum, test section, hump model, sheet-forming optics, and the laser sheet propagating through the test section. Figure 2(b) shows an end view of the optics and camera used to collect the Rayleigh and Raman signals. The diameter of lens L6 is 10 cm and the effective focal length is 82 cm, which gives an f/8 collection geometry. In the end view of figure 2(b), the flow is out of the plane of the paper towards the reader. The collection optics (L6 and mirrors M3 and M4) are located inside the plenum. All collection optics (including the camera) are omitted from figure 2(a) to avoid cluttering the figure.

Beam splitter BS1 picks off a small fraction of the beam to monitor with an integrating sphere and a photodiode. This signal is used to account for pulse-to-pulse fluctuations in the total pulse energy. After the sheet-forming lenses, another beam splitter BS2 is used to pick off a small fraction of the light sheet and project it onto a linear diode array. Since the distance from BS2 to the diode array is approximately the same as from BS2 to the observation volume near the model, the beam profile on the diode array can be used to normalize the raw images to spatial variations of intensity in the light sheet. This normalization method is the same as used previously (ref. 7). The polarization of the light sheet is such that the electric field lies in the plane of figure 2(a). The high-intensity laser sheet (140 mJ/pulse) is directed through the outer window into the plenum and then through slot S1 into the test section. The width of the laser sheet in the field of view is about 25 mm.

In many Rayleigh experiments reported in the literature, the viewing angle is perpendicular to the propagation direction of the beam and perpendicular to the plane of the light sheet. This geometry simplifies the geometrical interpretation of the acquired images and eliminates numerical image rotation in the post-processing of the data. Because of the geometrical constraints of the tunnel and model in this test, the light sheet is observed from a direction that is not perpendicular to the plane of the sheet or the propagation direction. The collection lens L6 looks down on the plane of the laser sheet with a viewing angle ϕ of about 20°. Since the angle θ that the beam makes with the test section wall is about 30°, the viewing angle of the detector significantly differs from the normal to the beam propagation (towards the backward direction).

The field-of-view (dotted rectangle in fig. 2(a)) of the camera is limited to regions upstream of M2 because the strong scatter from M2 can easily saturate the camera. Scattered background light on the detector is reduced with the following precautions. The horizontal slot S1 is 16.5 cm long in the streamwise direction and 1 cm tall. It is cut through the wall between the plenum and the test section to allow passage of the laser sheet into the test section without scattering from an additional window. One of the removable off-blocks from the model has been replaced with a dielectric mirror M2 to reflect the laser sheet downstream rather than let it impinge on the model surface. At the location where the laser sheet

strikes the tunnel wall, an absorbing neutral density filter is attached to the wall to minimize scatter upstream into the field of view of the detector.

There are three differences between the Raman and Rayleigh setups. The switch from Rayleigh to Raman is accomplished by inserting a band-pass interference filter (centered at 607 nm) in front of the intensified charge-coupled device (ICCD) camera. This filter attenuates the Rayleigh signal and scattered light at 532 nm but passes the 607-nm signal scattered from the vibrational mode of N_2. Second, L1 and L2 were removed from the sheet-forming optical train to reduce the width of the sheet in the observation region by a factor of two. Removing L1 and L2 improves the inherently weak Raman signal by increasing the laser intensity by a factor of two. Third, since the Raman signal is much smaller than the Rayleigh signal, we use a significantly higher gain on the camera intensifier for the Raman case.

Timing of Laser and Oscillatory Excitation

The image intensifier in the ICCD camera is gated with a width of 5 μs and timed to overlap the 8-ns laser pulse. However, because of the small SNR nature of the analog signal associated with the pressure pulse that drives the oscillatory excitation, the laser and camera could not be reliably triggered with a constant phase relative to the oscillatory excitation. We were forced to let the laser fire at 10 Hz, independently of the oscillatory flow. Hence the oscillatory flow through slot S2, which is executed at 200–800 Hz, is not phase locked to the laser light pulses.

To measure the time interval between each laser shot and the injection phase of the oscillatory excitation, a dynamic pressure transducer, located inside the hump-model cavity, was used to record the pressure fluctuations due to the oscillatory blowing valve. For each laser pulse, the temporal profiles of the laser light (from the integrating-sphere photodiode) and the pressure transducer are digitized and recorded with a multichannel oscilloscope. By comparing these two digitized temporal signals during post-processing of the data, the timing of each laser pulse relative to the injection phase of the oscillatory flow can be unambiguously determined.

A typical data set consists of 44 consecutive images taken at 10 Hz. For each laser pulse, the ICCD camera image, diode array profile of the laser sheet, and the integrating-sphere photodiode signal are stored in an IBM compatible PC. Chance determines whether each image is acquired during the fluid injection phase or is completely out of phase with the injection time. Many of the 44 images are acquired out of phase with fluid injection and are not of interest, except as a reference image with no injection. By chance, a few of these 44 images are acquired near the fluid injection time. In these few images, we expect to see flow structure as a result of the oscillatory excitation.

Laboratory Results

To test the equipment and experimental design before attempting the planar imaging in the facility, the experiment was set up in the laboratory by using about the same laser energy/pulse, geometry, beam-path lengths, lenses, and data acquisition that we used in the TCT. Sheets of metal and aluminum foil were used to simulate the model surface that would be present in the TCT configuration.

In figure 3, two averaged (44 laser shots or 4.4 sec) images of the laser light sheet in room air (300 K and 10^5 Pa) from the laboratory are compared. Figure 3(a) shows Raman scattering, while figure 3(b) shows Rayleigh scattering. The only differences in the setup used to obtain these images are the same three changes described previously for conversion from Rayleigh to Raman. The Rayleigh sheet width (25 mm) in figure 3(b) is twice the width of the sheet for the Raman image in figure 3(a). In each image,

the sheet signal, minus background, is proportional to the density. The noise in the Raman image is predominately dark noise from the detector because of the relatively low light level of the Raman scatter. The 532-nm signal for Rayleigh is much larger than the Raman 607-nm signal, but the noise is also much larger, dominated by the scattered stray light at 532 nm. The laser energy is 140 mJ/pulse.

Detection Limits

From the averaged images of figure 3, we estimate the detection limits for both Rayleigh and Raman scattering in the unseeded air sample for our laser energies and experimental geometry. The detection limit is defined as an SNR ~ 1. We observe an SNR of 15 for Rayleigh scattering (fig. 3b) and an SNR of 1 for Raman scattering (fig. 3(a)). Since both signals are acquired from one atmosphere of room air, the detection limits are about 2×10^{18} cm^{-3} for Rayleigh scatter and 3×10^{19} cm^{-3} for Raman scatter. Since these estimates are for averages of 44 images, single pulse detection limits are about $\sqrt{44} \approx 6$ times larger. In the current work, with Rayleigh scattering averaged over 44 pulses, the detection limit is about ten times smaller than the limit that we estimate from our previous (ref. 3) work, which used an 80-mW cw laser with the same wavelength and about the same averaging time. Considering measurement uncertainties, this improvement of a factor of ten in detection limit is consistent with an increase in average laser power of 17.

TCT Results

One difference between the Rayleigh laboratory and TCT work was that portions of the TCT model surface were curved, and these curved regions reflected and crudely focused some stray light into our collection optics. The model/tunnel geometry forced us to work with this high background level, which reduced the SNR and increased the detection limit, relative to that stated above for laboratory conditions. This high background was not a problem with the Raman signal because of the interference filter. In spite of the extra background, the Rayleigh SNR was ≥ than the Raman SNR.

Raman imaging was performed at the TCT with the hump model installed and no flow. The test section contained room air. The quality of these Raman images was about the same as for the laboratory Raman images. Placing a second filter (a colored glass, long-pass filter), along with the first interference filter, in front of the camera did not reduce the background level. Thus, the limiting noise on the Raman images was the camera dark current and shot noise and was not scattered 532-nm light as it was for the Rayleigh images. Typical TCT run conditions have ten times the density of room air. Thus, we expect ten times the Raman signal and SNR for typical run conditions compared to the room air results. We did not pursue Raman imaging further in the TCT because of a lack of time; however, planar Raman imaging is clearly possible in this facility.

A second difference between the laboratory work and the TCT work is that the TCT results show a strong degree of streaking in the planar Rayleigh images. These streaks show a strong pulse-to-pulse variation. They are not due to density structures in the flow that we are imaging but are the result of streaking in the laser light sheet. The streaks and their temporal variation were not present in the laboratory data and were not present in the TCT data when the test section was filled with room air.

The streaking of the laser light sheet was produced after the sheet passed through the window W2. To verify this, the diode array in figure 2(a) records the laser sheet profile before the laser sheet enters the tunnel. Figure 4 shows a typical example of the intensity across the width of the laser sheet on the diode array. This example is from the setup at TCT, while running, but is similar to those sheet profiles observed in the laboratory. The peaked structure of the sheet profile of figure 4 is due to a combination of

the doughnut spatial mode of the laser, focusing it into a sheet, and imperfections in the laser mode. The single shot laser light sheet profiles were approximately constant and repeatable over any set of 44 images and over the several-month duration of this work. Thus, there was no time dependence of the sheet width profile observed on the diode array, which confirms that, with the tunnel running, the streaks were not imbedded on the laser sheet coming directly from the laser.

The perturbations to the light sheet are illustrated in figure 5, with the facility running at free-stream conditions: Mach 0.2, 3×10^5 Pa, 150 K. Six single-shot Rayleigh images are shown. Compare figures 5(a)–5(c) (unseeded) with figures 6(d)–6(f) (CO_2 seeding) to see the improvement in image quality with seeding. The broad vertical lines in figures 5(a)–5(c), stray scattered light off the model, are eliminated in the seeded cases of figures 5(d)–5(f) because the scattered signal from the light sheet is larger, relative to the scatter from the model surfaces. In spite of this significant perturbation (streaking) to the laser beam, we tried to use these light sheets to observe fluid injection with the hump model.

Application to Oscillatory Excitation

Boundary layer control, including the prevention or delay of flow separation from a confining surface, has been studied for many years. Steady blowing, steady suction, and oscillatory excitation are three techniques that are used. Early work (refs. 8 and 9) with oscillatory excitation at low Reynolds number was followed by demonstrations (ref. 10) at higher Reynolds numbers in the TCT. Recently, flow over an airfoil was simulated (ref. 6) by mounting a hump on the vertical wall of an otherwise empty tunnel (see fig. 1). This setup was designed to study oscillatory excitation and its effect on flow separation at free-stream conditions of Mach 0.2, 150 K, and 5×10^5 Pa.

To demonstrate an application of planar Rayleigh imaging in the TCT, we used this hump model to visualize the flow just downstream of the slot S2, looking for transient flow features (e.g., vortex shedding) that may result from the oscillatory excitation through the slot. The ratio for the densities of the colder free-stream fluid and the warmer fluid injected through the slot S2 is two, thus we expect, at best, a factor of two for the fractional change in density $\Delta\rho/\rho$ across the vortex of mixing fluid near the injection slot. This density gradient should be detectable without seeding, based on the detection limit given above.

Figure 6 contains three instantaneous images (using CO_2 seeding) showing three different instances of transient flow structure due to weak oscillatory excitation. These three cases come from a larger set of 44 laser shots, where the other 41 shots show no sign of flow structure. The figure 6(a) image shows a single laser shot that contains a weakly scattering feature. The figure 6(b) image shows another single-pulse example of flow structure (much stronger than in fig. 6(a)) in the same location, and figure 6(c) shows a third moderately scattering structure. The position of these three features is about 1–2 cm (or less) off the wall and is shown by the small shaded ellipse within the camera's field-of-view (dotted rectangle) in figure 2(a). For reference, images (figs. 6(d), 6(e), and 6(f)) show the laser shots immediately before (0.1 sec) each of the shots used for figures 6(a)–6(c), respectively. All three reference images show no observable feature.

The timing of the three examples of flow features shown in figures 6(a)–6(c) provides evidence that the observed features are due to the oscillatory excitation. All three occur at approximately the same relative time with respect to the maximum pressure in the hump model cavity. The time delay Δt is a measure of the time between the maximum of the pressure pulse inside the model and the laser pulse and is specified in the figure for each of the six images. The frequency of oscillatory excitation for the data of figure 6 is 205 Hz; thus, the period is 5 msec, and we expect unsteady fluid flow with this same period.

6

Images (a) through (c) in figure 6 that contain the features have delays in the range of 3–4.5 msec, while the reference images (d) through (f), without features, have delays in the range of 1.5–3 msec. Thus, these six images are self consistent in the sense that all three possible flow structures appear in the same half of phase space, while all three reference images, without flow structure, are representative of the opposite half (i.e., ~180° out of phase). This result is consistent with an expectation of seeing something during only one half of the oscillatory excitation period.

Degradation of the Laser Light Sheet

The streaking of the light sheet that was observed throughout the test, when the facility was running with typical cryogenic conditions, is likely generated by the fluid inside the tunnel since it is not evident on the diode array data. These streaks are not due to absorption or attenuation of the laser beam inside the wind tunnel. To test for absorption, we calculate the integrated signal over the laser sheet width for each laser pulse. In figure 5(a), a dotted vertical line shows the column (i.e., position) where this integration is carried out. Figure 7 shows two examples ((a) no seeding and (b) seeding of CO_2) of integrating over the profile of the light sheet at this particular location. Each data point in the figures is the result of integration over the sheet width for one laser shot, with the background subtracted. Each figure shows the results for a series of 44 successive laser shots (i.e., 4.4 sec of data). Because the signal with seeding is much greater than the signal without seeding, the camera gain is reduced for the case of figure 7(b) compared to figure 7(a).

The unseeded data of figure 7(a) show that the integrated signal (over the sheet width) is constant with laser shot number or time and that the shot-to-shot variations are about 20 percent. This percentage is greater than the pulse-to-pulse variations in the pulse energy, which were measured to be 10 percent when using the integrating sphere and photodiode. The signal variations are larger because the small Rayleigh signal contains stray background and shot noise. The seeded data of figure 7(b) show a steady increase in the signal level. This steady increase is due to an increase in CO_2 seed density over 4.4 sec. In this setup, we have only crude adjustment of the seed rate and cannot easily control the temporal stability of the seeded signal. However, over short time periods (~0.5 sec) containing several pulses, the data show that the integrated signal is roughly constant, whereas the streaks in figure 5 are changing every pulse. Thus, for both unseeded and seeded conditions, the total integrated light-sheet energy is not changing on a pulse-to-pulse basis. Thus, the streaks arise with beam steering from index of refraction perturbations and not from absorption.

Four possible causes for index of refraction variations are noted. First, assuming isentropic Mach 0.2 flow and a recovery factor of one, the fractional density gradients in the test section would be $d\rho/\rho \leq$ 1 percent, if the flow were completely stagnated. It is unlikely that these small density gradients could cause the large effects seen in figures 5 and 6.

Second, did the slot S1 that was cut between the test section and the plenum cause boundary layer perturbations and hence the beam fluctuations of figure 5? The plenum pressure is typically <2 percent larger than the test-section pressure. With the slot S1, a weak jet is created from the plenum into the test section; however, the density gradients in this jet are also small and unlikely to cause the intense striations in figures 5 and 6. Additionally, in previous (ref. 3) work, we observed excessive beam steering of a laser beam (not a light sheet) without cutting holes in the test section walls (i.e., with windows on both sides of the test section) in this same facility.

A third possibility is temperature gradients in the plenum. Previous work (ref. 11) attributed thermal gradients in the plenum as the cause of image distortion in flow visualization at the TCT. This cause is roughly consistent with the streaking of figures 5 and 6.

A fourth possibility is the turbulent boundary layer region of the test section. If the perturbation is assumed to occur over a very short (localized) distance of path length, it is easy to visualize the generation of approximately parallel streaks, as seen in figures 5 and 6. The boundary layer at slot S1 is a likely candidate for this region. The effect of this perturbation is then observed downstream in the laser sheet near the model. What could provide the index-of-refraction variation necessary to steer the beam? Over the course of this work and previous (ref. 3) work, we have observed a trend. Whenever the cryogenic flow is stagnated, we observe the generation of clusters in the fluid with Rayleigh instrumentation. Although we cannot conceive of a thermodynamic argument that predicts cluster formation in the boundary layer, we speculate that the boundary layer, which is effectively stagnated, may also contain sufficient clusters to provide the necessary index-of-refraction gradients to steer the beam. There is a second possibility related to clustering. In previous work (ref. 3), we typically observed clusters in the plenum, even though the free stream was free of clusters. Possibly, clusters are simply being sucked through slot S1 into the test section boundary layer region.

Summary of Results

1. Off-body flow visualization of density, with planar Rayleigh scattering, was performed in the unseeded 0.3-Meter Transonic Cryogenic Tunnel (TCT).

2. Planar Raman imaging was also shown to be feasible in the unseeded TCT.

3. By seeding CO_2 into the flow, clustering was induced and provided a significant enhancement of the Rayleigh flow visualization.

4. Planar Rayleigh imaging with seeding was used to observe transient flow structure due to vortex shedding in the wake of an oscillatory blowing slot.

5. The cryogenic fluid perturbs the intensity profile of the laser light sheet with streaks and degrades the quality of the flow visualization.

8

References

1. Herring, G. C.; and Hillard, Jr., M. E.: *Flow Visualization by Elastic Light Scattering in the Boundary Layer of a Supersonic Flow*. NASA TM-210121, Aug. 2000.

2. Escoda, M. C.; and Long, M. B.: Rayleigh Scattering Measurements of the Gas Concentration in Turbulent Fields, *AIAA Journal*, vol. 21, 1983, pp. 81–84.

3. Shirinzadeh, B.; and Herring, G. C.: *Demonstration of Imaging Flow Diagnostics Using Rayleigh Scattering in Langley 0.3-Meter Transonic Cryogenic Tunnel*. NASA TM-208970, Feb. 1999.

4. Eckbreth, A. C.: *Laser Diagnostics for Combustion Temperature and Species*. Abacus (Cambridge, MA) 1988, Chapter 5.

5. Balakriskna, S.; and Kilgore, W. A.: *Performance of the 1/3-Meter Transonic Cryogenic Tunnel with Air, Nitrogen, and Sulfur Hexafluoride Media Under Closed Loop Control*. NASA CR-195052, Jan. 1995.

6. Seifert, A.; and Pack, L. G.: Active Control of Separated Flows on Generic Configurations at High Reynolds Numbers. *AIAA 99-3403*, June–July 1999.

7. Shirinzadeh, B.; Balla, R. Jeffrey; and Hillard, M. E.: Rayleigh Scattering in Supersonic Facilities. *AIAA 96-2187*, June 1996.

8. Katz, Y.; Nishri, B.; and Wygnanski, I.: The Delay of Turbulent Boundary Layer Separation by Oscillatory Active Control. *Phys. Fluids A*, vol. 1, 1988, pp. 179–181.

9. Seifert, A.; Bachar, T.; Koss, D.; Shepshelovich, M.; and Wygnanski, I.: Oscillatory Blowing: A Tool to Delay Boundary-Layer Separation. *AIAA Journal*, vol. 31, 1993, pp. 2052–2060.

10. Seifert, A.; and Pack, L. G.: Oscillatory Control of Separation at High Reynolds Numbers. *AIAA-98-0214*, Jan. 1998.

11. Snow, W. L.; Burner, A. W.; and Goad, W. K.: *Improvement in the Quality of Flow Visualization in the Langley 0.3-Meter Transonic Cryogenic Tunnel*. NASA TM-87730, 1986.
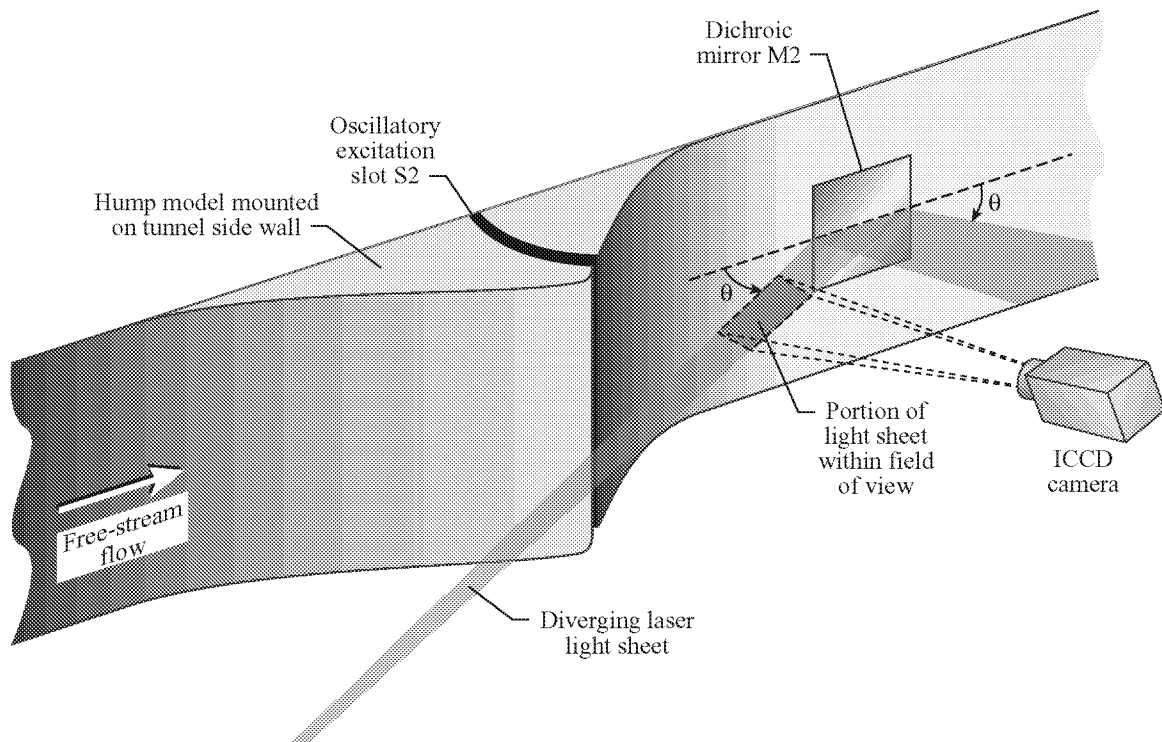
Figure 1. Overview of planar light scattering at the 0.3-Meter Transonic Cryogenic Tunnel (TCT). (ICCD stands for intensified, charge-coupled device.)
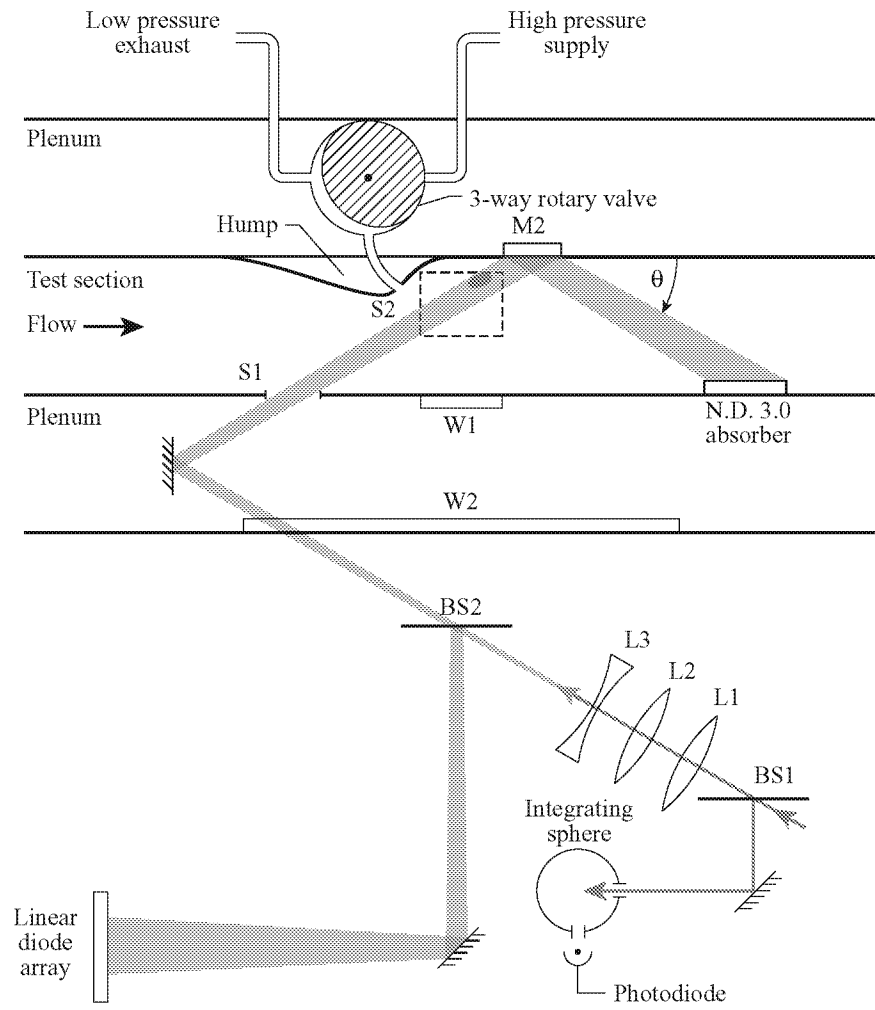
(a) Top view.
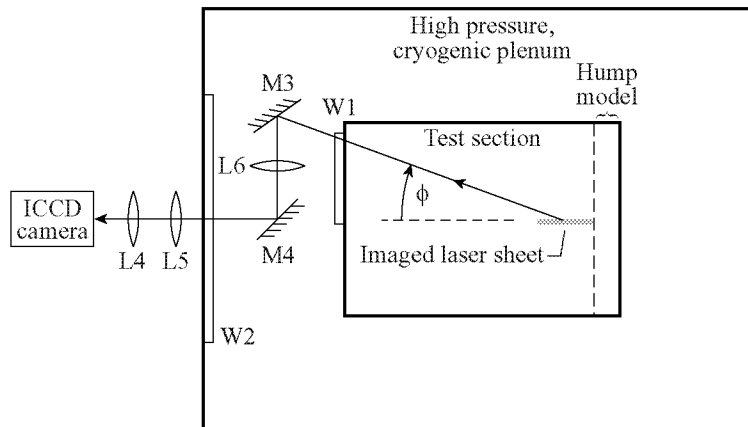
(b) End view.

Figure 2. Schematic of the experimental setup at the TCT.

11
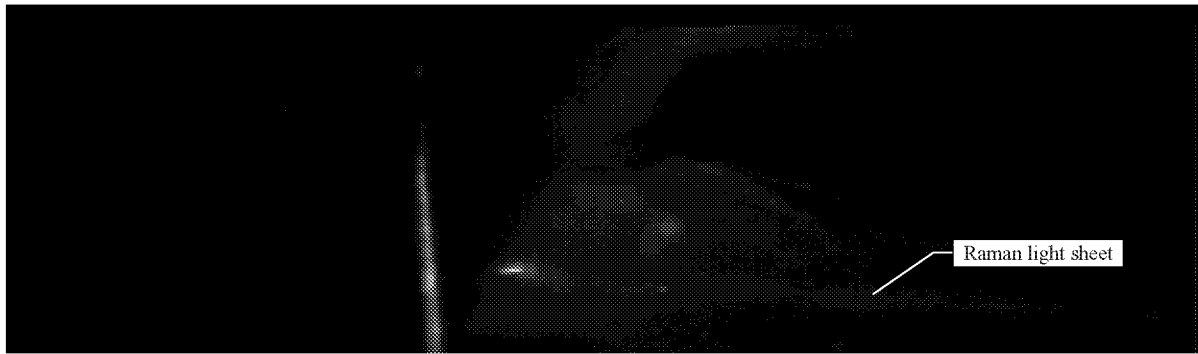
(a) Raman light sheet.
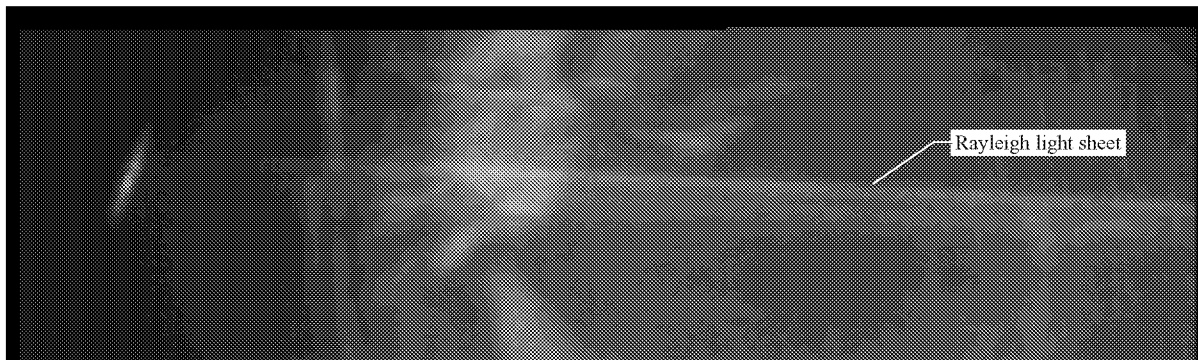
(b) Rayleigh light sheet.

Figure 3. Examples of averaged (44 shots) images for (a) Raman and (b) Rayleigh light sheets in laboratory room air using setup equivalent to TCT setup.
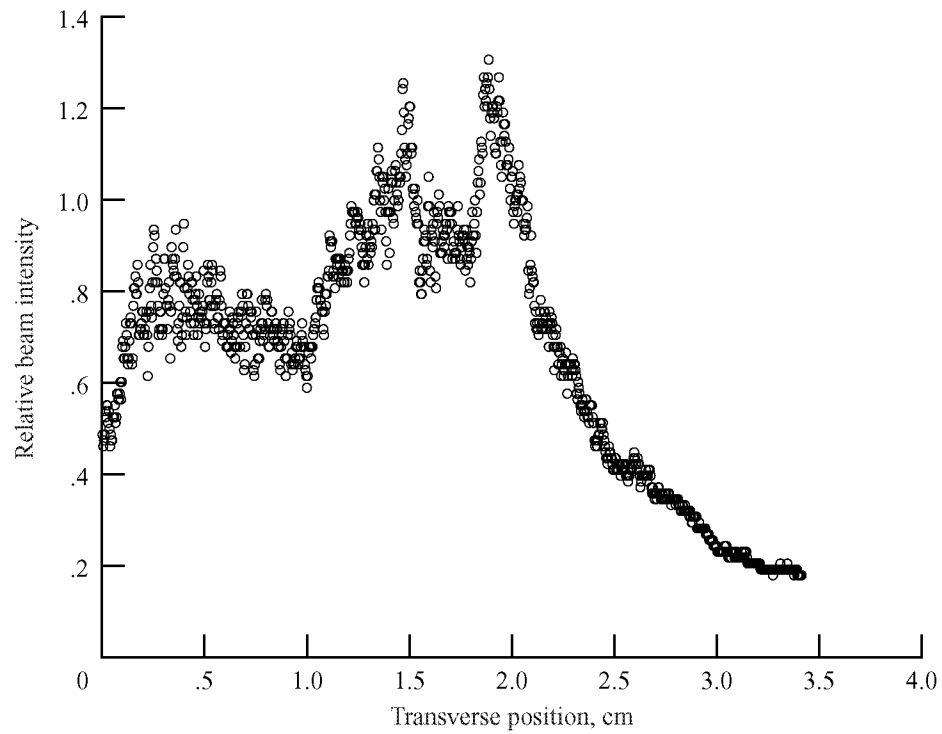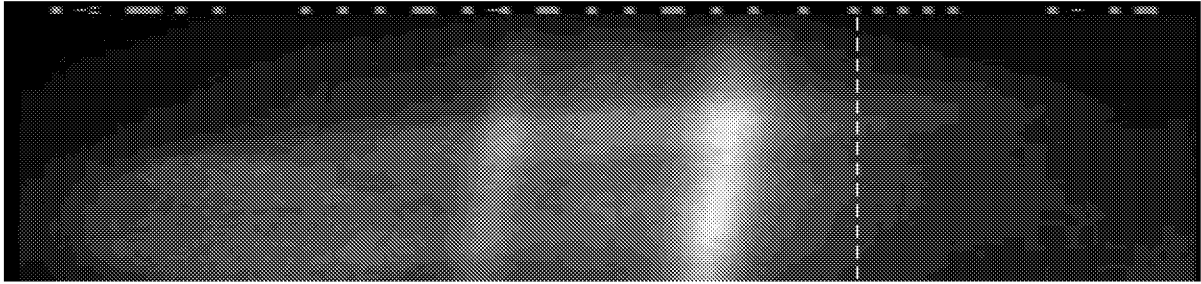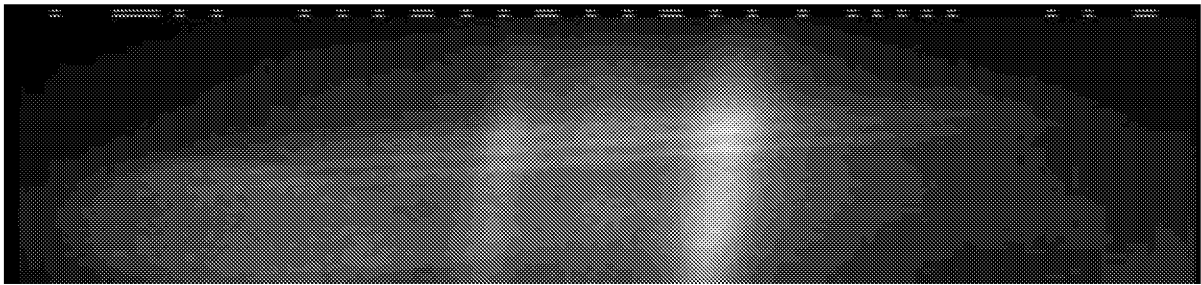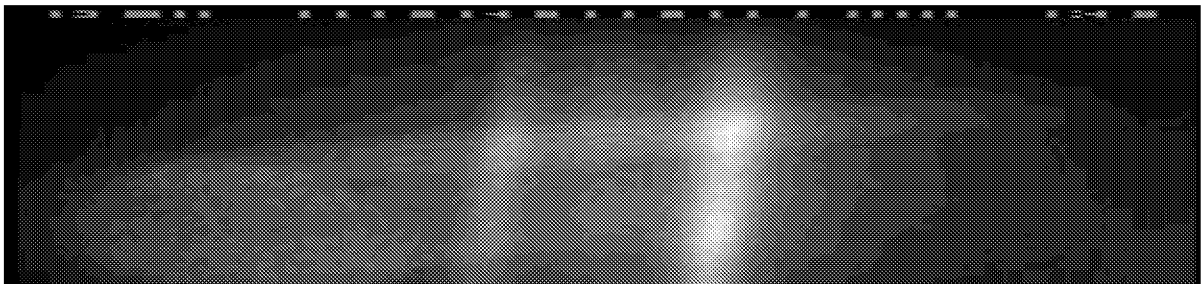
Figure 4. Single-pulse intensity profile across width of laser light sheet, measured on diode array while tunnel is running under typical conditions.

(a) CO_2 seeding not used.

(b) No seeding.

(c) No seeding.

Figure 5. Six single shots of Rayleigh images of flow near hump model. ICCD intensifier gain is significantly larger for unseeded cases (a–c).
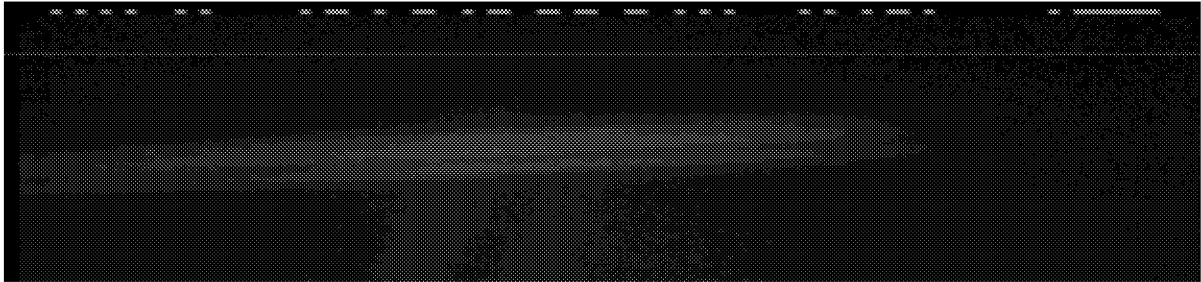
(d) With CO_2 seeding.
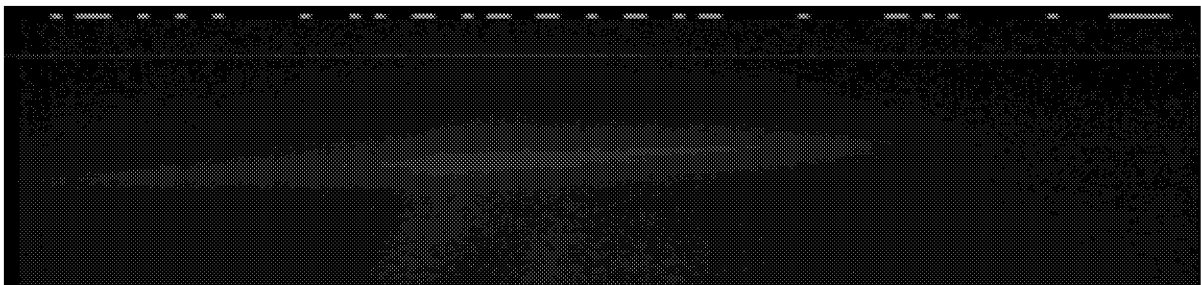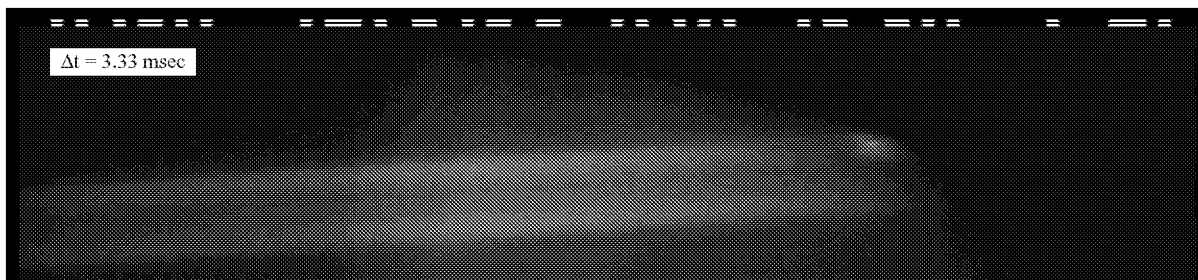

(e) With seeding.
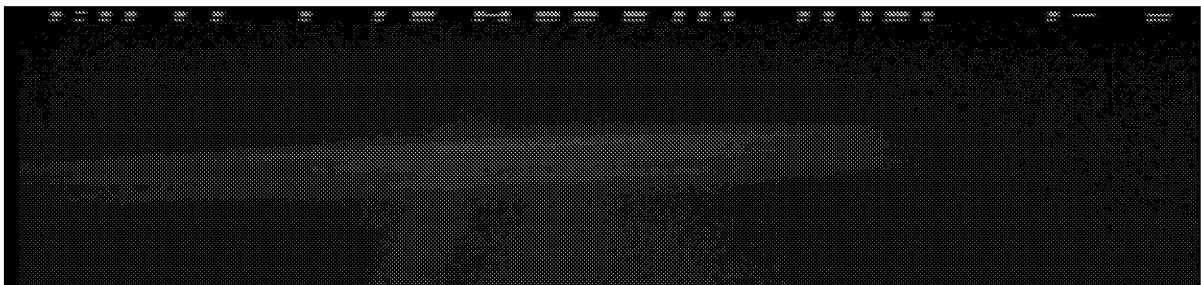
(f) With seeding.

Figure 5. Concluded.

15
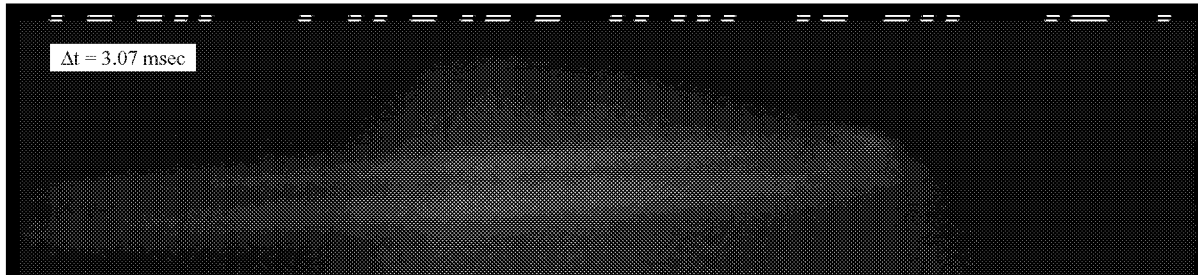
(a) Weak scattering.
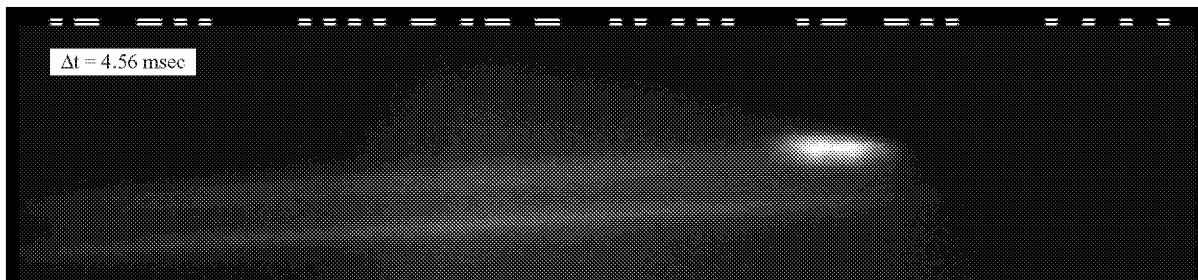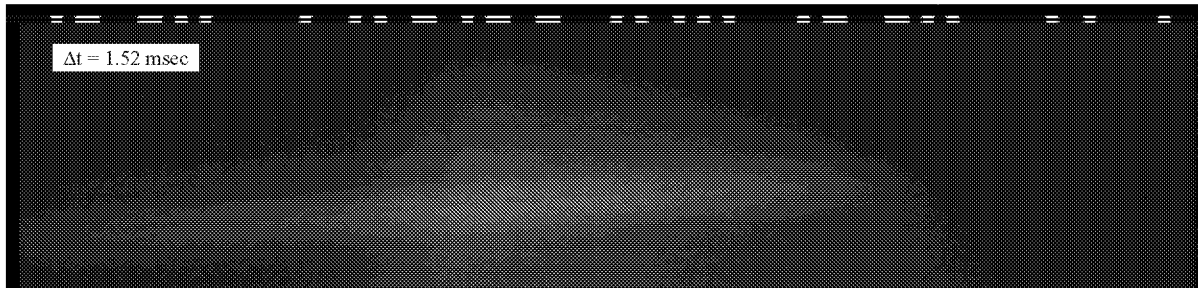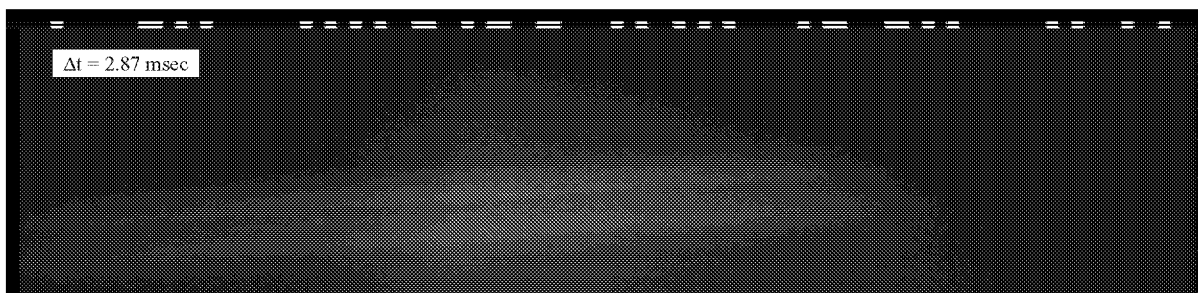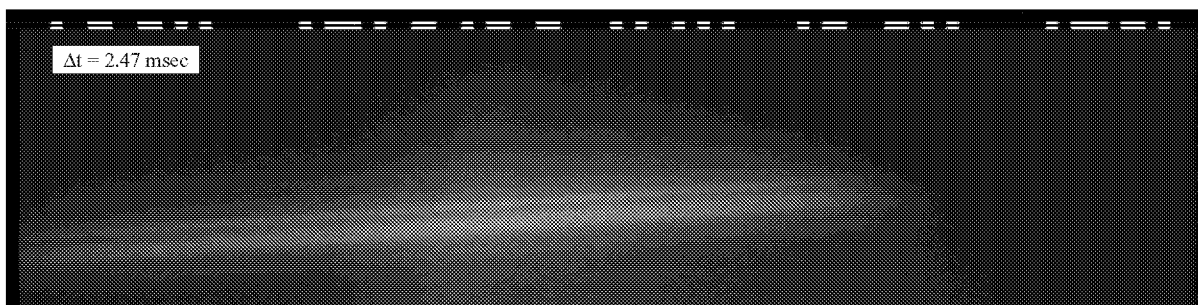

(b) Strong scattering.

(c) Moderate scattering.

Figure 6. Three examples of Rayleigh (with seeding of CO_2) single shots that show flow structure (due to oscillatory excitation) slightly downstream of slot S2.
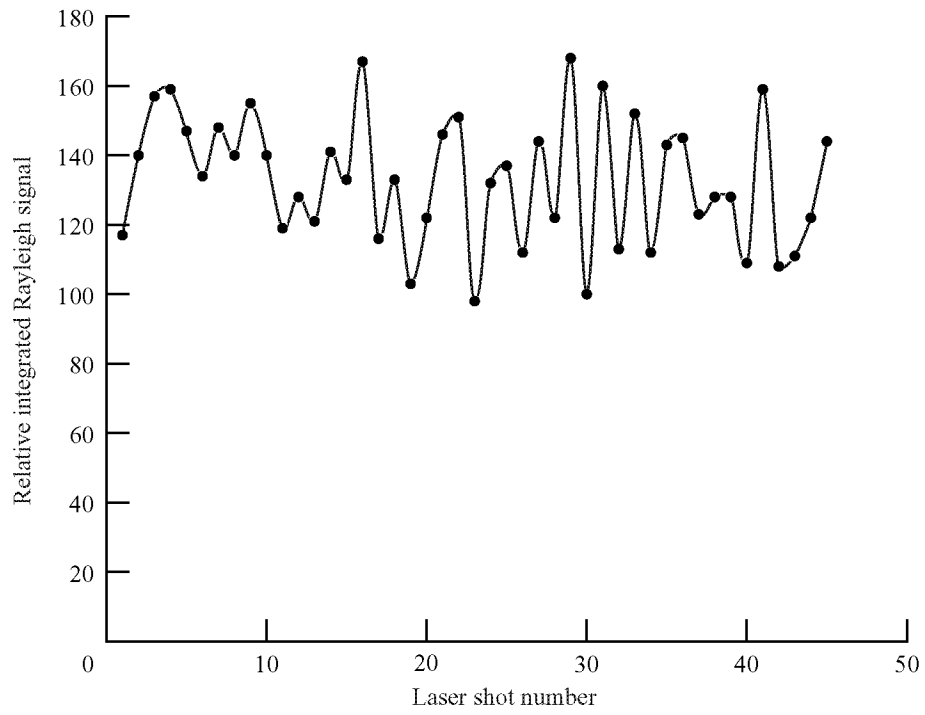
(d) 0.1 sec before (a).
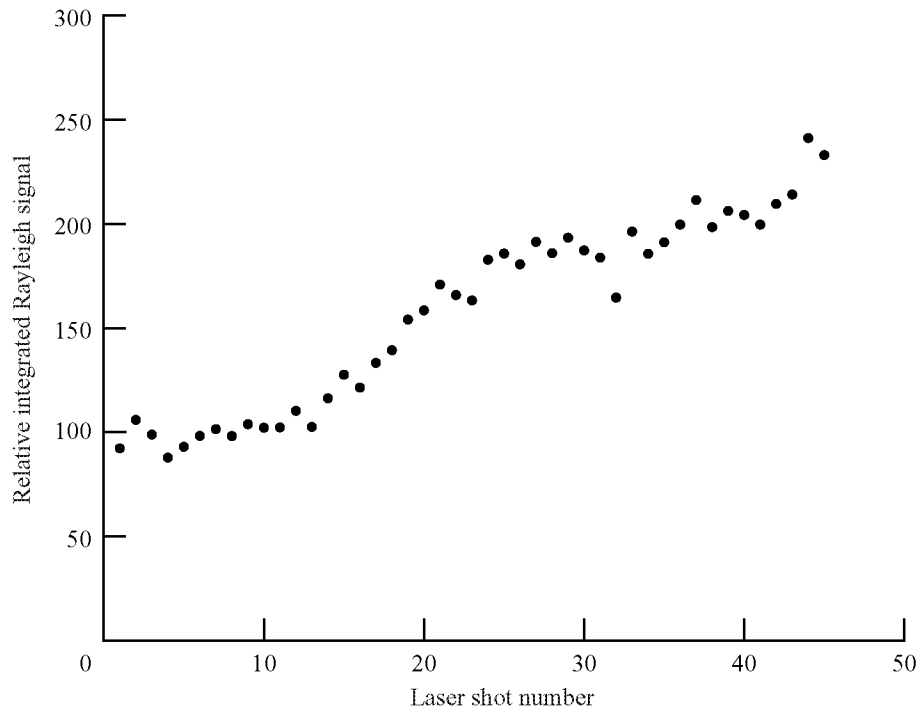

(e) 0.1 sec before (b).

(f) 0.1 sec before (c).

Figure 6. Concluded.

17

(a) Unseeded.

(b) Seeding with CO_2.

Figure 7. Two examples of the shot-to-shot fluctuations of Rayleigh signal integrated over width of laser sheet.

REPORT DOCUMENTATION PAGE

Public reporting burden for this collection of information is estimated to average 1 hour per response, including the time for reviewing instructions, searching existing data sources, gathering and maintaining the data needed, and completing and reviewing the collection of information. Send comments regarding this burden estimate or any other aspect of this collection of information, including suggestions for reducing this burden, to Washington Headquarters Services, Directorate for Information Operations and Reports, 1215 Jefferson Davis Highway, Suite 1204, Arlington, VA 22202-4302, and to the Office of Management and Budget, Paperwork Reduction Project (0704-0188), Washington, DC 20503.

1. AGENCY USE ONLY *(Leave blank)*	2. REPORT DATE	3. REPORT TYPE AND DATES COVERED
	June 2002	Technical Memorandum

4. TITLE AND SUBTITLE
Flow Visualization of Density in a Cryogenic Wind Tunnel Using Planar Rayleigh and Raman Scattering

5. FUNDING NUMBERS
WU 706-31-11-01

6. AUTHOR(S)
Gregory C. Herring and Behrooz Shirinzadeh

7. PERFORMING ORGANIZATION NAME(S) AND ADDRESS(ES)

NASA Langley Research Center
Hampton, VA 23681-2199

8. PERFORMING ORGANIZATION REPORT NUMBER

L-18171

9. SPONSORING/MONITORING AGENCY NAME(S) AND ADDRESS(ES)

National Aeronautics and Space Administration
Washington, DC 20546-0001

10. SPONSORING/MONITORING AGENCY REPORT NUMBER

NASA/TM-2002-211630

11. SUPPLEMENTARY NOTES

12a. DISTRIBUTION/AVAILABILITY STATEMENT

Unclassified—Unlimited
Subject Category 74   Distribution: Standard
Availability: NASA CASI (301) 621-0390

12b. DISTRIBUTION CODE

13. ABSTRACT *(Maximum 200 words)*
Using a pulsed Nd:YAG laser (532 nm) and a gated, intensified charge-coupled device, planar Rayleigh and Raman scattering techniques have been used to visualize the unseeded Mach 0.2 flow density in a 0.3-meter transonic cryogenic wind tunnel. Detection limits are determined for density measurements by using both unseeded Rayleigh and Raman (N_2 vibrational) methods. Seeding with CO_2 improved the Rayleigh flow visualization at temperatures below 150 K. The seeded Rayleigh version was used to demonstrate the observation of transient flow features in a separated boundary layer region, which was excited with an oscillatory jet. Finally, a significant degradation of the laser light sheet, in this cryogenic facility, is discussed.

14. SUBJECT TERMS
Rayleigh scattering; Raman scattering; Cryogenic Wind Tunnel

15. NUMBER OF PAGES
23

16. PRICE CODE

17. SECURITY CLASSIFICATION OF REPORT	18. SECURITY CLASSIFICATION OF THIS PAGE	19. SECURITY CLASSIFICATION OF ABSTRACT	20. LIMITATION OF ABSTRACT
Unclassified	Unclassified	Unclassified	UL

NSN 7540-01-280-5500